Negative linear compressibility and phonon softening in $Mg(IO_3)_2$ under pressure

F. Bodo [1,2] E. Kraka [1] and A. Erba [2,*]

[1] *Computational and Theoretical Chemistry Group (CATCO), Department of Chemistry, Southern Methodist University, Dallas, Texas 75275-0314, USA*

[2] *Dipartimento di Chimica, Università di Torino, via Giuria 5, 10125 Torino, Italy*

(Received 20 October 2025; revised 4 December 2025; accepted 16 December 2025; published 12 January 2026)

We investigate pressure-induced changes in the structure, lattice dynamics, mechanical properties, and bonding of the strongly anisotropic, monoclinic $P2_1$ phase of $Mg(IO_3)_2$ via the density functional theory with a global hybrid density functional approximation. Infrared and Raman spectra are simulated, which highlight a peculiar pressure-induced phonon softening of certain bands assigned to I-O stretching modes. As pressure increases, a redistribution of the electron density around the iodine atoms is observed leading to the elongation and weakening of the three I-O interactions within $[IO_3]$ structural units, with a corresponding pressure-induced expansion of the **a** and **c** lattice vectors, which translates into a negative linear compressibility of the material in the **ac** plane. This is accompanied by the shortening and strengthening of the interaction of iodine atoms with their three second-neighboring oxygen atoms, with a corresponding compression of the **b** lattice vector along which they are mainly oriented. Quasiharmonic lattice dynamical calculations reveal a negative thermal expansion in the **ac** plane. The strength of various interatomic interactions, as well as their evolution with pressure, is assessed in terms of local mode adiabatic force constants obtained through a new periodic implementation of the local vibrational mode theory. We complement and corroborate the analysis with a topological description of the electron density through the quantum theory of atoms in molecules.

DOI: 10.1103/f9bp-9ggw

I. INTRODUCTION

In recent years, metal iodates have been attracting attention because of their peculiar structural and electronic properties [1–5]. The growing interest in new generation materials for nonlinear optics (NLO) and second-harmonic generation (SHG) [6–15,15,16] has led to the synthesis and characterization of metal iodates based on new cations, including alkali metals, alkaline earth metals [11,17–19], transition and post-transition metals [8,19], and lanthanides [10,20,21]. Many of these properties are a direct consequence of the noncentrosymmetric structure of the majority of these systems [5,12,22]. Moreover, the $[IO_3]^{-1}$ units, usually arranged in a trigonal pyramid, possess a lone electron pair (LEP) located on the iodine atoms, leading to an asymmetric oxygen environment for both the iodine and the metal cation, further enhancing these properties through enhanced polarization [1,3,23]. The manipulation of the direction of such polarization becomes key to favoring the SHG response of the material. As an example, the introduction of iodate units within the borate framework [24] or the tetraiodatoiodate unit in KIO_3 [25] have yielded an enhanced SHG response. Another viable way to tune and improve iodate properties is the use of pressure; the presence of the LEP on the iodine atom, in fact, favors the formation of so-called halogen bonds [26–29], which play a key role in stabilizing the iodate structure. These electrostatic interactions are particularly sensitive to pressure, which becomes an effective medium to tune the SHG response and NLO properties [4]. Pressure tuning has indeed allowed us to better understand the role of the iodine LEP in the chemical bonding of these materials [3,4,16,23,30,31].

In 2022, Liang *et al.* [23] synthesized crystals of $Mg(IO_3)_2$ and studied their behavior under pressure by collecting x-ray diffraction (XRD) patterns, as well as Raman and infrared (IR) spectra up to ∼20 GPa. The results indicate that the structure of $Mg(IO_3)_2$ changes significantly under compression and that the system eventually undergoes a phase transition from the monoclinic $P2_1$ space group to the trigonal $P3$ space group between 7.5 and 9.7 GPa. While bond lengths typically decrease upon compression—with an associated increase in the bond strength—vibrational spectroscopic evidence suggested otherwise, with certain peaks in the IR and Raman spectra assigned to I-O stretching modes being redshifted upon compression, thus suggesting bond softening rather than strengthening. At ambient pressure, the structure of $Mg(IO_3)_2$ is characterized by IO_3 trigonal pyramidal units, where each iodine atom participates in three strong interactions with three first-neighboring (fn) oxygen atoms (with bond lengths $I\text{-}O_{fn} \sim 1.9$ Å) and, through its LEP, in three weaker interactions with three second-neighboring (sn) oxygen atoms (with bond lengths $I\text{-}O_{sn} \sim 2.7$ Å). Each oxygen atom in the IO_3 unit acts as a linker to the Mg counterions, producing a distorted MgO_6 octahedron, which results in an anisotropic and compressible environment that is largely sensitive to external stimuli [3,22,23]. The crystal structure of $Mg(IO_3)_2$ in its monoclinic phase with $P2_1$ space group is reported in Fig. 1.

While the exact evolution with pressure of the individual atomic positions could not be experimentally refined [23], the above-mentioned spectroscopic evidence suggests that the $I\text{-}O_{fn}$ bonds get elongated as pressure increases, reflecting the

*Contact author: alessandro.erba@unito.it

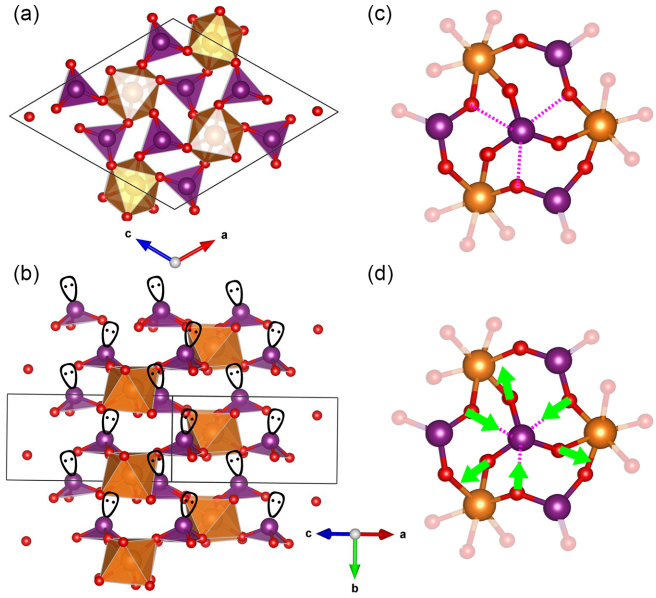

FIG. 1. (a), (b) Crystal structure of $Mg(IO_3)_2$ in its monoclinic phase with $P2_1$ space group; distorted MgO_6 octahedra are highlighted in brown and trigonal pyramidal IO_3 units in violet. (c) Schematic representation of the chemical bonding pattern around an iodine atom, with three strong interactions with first-neighboring oxygen atoms, and three weak interactions (marked by dashed magenta lines) with second-neighboring oxygen atoms. (d) Green arrows schematically represent the effect of pressure on the bond length of the different I-O interactions.

weakening of the corresponding chemical interaction upon compression, likely accompanied by the strengthening of the I-O_{sn} interactions.

In this study, we investigate the evolution with pressure of the structure, lattice dynamics, mechanical response, and bonding in $Mg(IO_3)_2$ with density functional theory (DFT) simulations, through the use of a global hybrid density functional approximation. From the computed fourth-rank elastic tensor, a negative linear compressibility (NLC) of the material in the **ac** plane is predicted. Materials with a NLC usually exhibit a variety of anomalous effects, such as negative thermal expansion, a negative Poisson's ratio, phonon softening upon compression, and phase transitions, and they have been attracting attention for many technological applications [32–37].

Simulated IR and Raman spectra fully capture the observed pressure-induced phonon-softening of I-O_{fn} stretching bands. We quantify the evolution with pressure of the strength of I-O_{fn} and I-O_{sn} interactions with the local vibrational mode theory (LVMT) [38,39], with our new periodic implementation in the CRYSTAL electronic structure program [40]. The LVMT represents an effective way to decompose complex normal modes in vibrational spectroscopy of molecules [38,39,41] and materials [28,42,43] into simpler, localized modes associated with specific bonds or internal coordinates. This decomposition provides a quantitative measure of bond strength (the local mode adiabatic force constant), and offers a simple way to analyze vibrational spectra in terms of local structural units. We complement the LVMT analysis with a topological description of the electron density through the quantum theory of atoms in molecules (QTAIM) [44,45].

II. FORMAL AND COMPUTATIONAL ASPECTS

A. Linear compressibility

The elastic response of a material can be described in terms of a fourth-rank elastic stiffness tensor $\mathbf{C}$, with elements C_{ijkl} (with $i, j, k, l = x, y, z$)—i.e., elastic constants—defined as second energy derivatives with respect to pairs of lattice deformations [46]:

$$C_{ijkl} = \frac{1}{V}\frac{\partial^2 E}{\partial \eta_{ij}\eta_{kl}}\bigg|_{\eta=0}, \tag{1}$$

where $\boldsymbol{\eta}$ is the lattice strain tensor and V is the equilibrium volume. We compute the elastic constants in Eq. (1) as numerical derivatives of analytical forces [47–51]. A variety of mechanical elastic properties of a crystal can be evaluated from $\mathbf{C}$, including the Young modulus E (i.e., the strain response of a solid to a uniaxial stress, in the direction of the stress), the linear compressibility β (i.e., the linear strain under the application of an external hydrostatic stress), the shear modulus G (i.e., the strain response to a shear stress), and Poisson's ratio ν (i.e., the strain response in the directions orthogonal to a uniaxial stress) [52].

The value of the linear compressibility β of a crystal can be computed along any direction in space (identified by a Cartesian vector $\mathbf{v}$ or, equivalently, in terms of two angles ϑ and φ in spherical coordinates) as [53]

$$\beta(\vartheta, \varphi) = S_{ijkk} v_i v_j, \tag{2}$$

where Einstein's notation is used according to which indices that are repeated are meant to be summed over, and where S_{ijkl} are the elements of the inverse of the elastic tensor $\mathbf{S} = \mathbf{C}^{-1}$.

B. Local modes in periodic systems

We describe the harmonic lattice dynamics of a periodic crystal within a direct-space, frozen-phonon approach, where second-order interatomic force constants are computed by displacing atoms in the reference lattice cell and by evaluating analytically the forces acting on all atoms within a supercell (SC) [54]:

$$H^{\mathbf{g}}_{ij} = \frac{\partial^2 E}{\partial u^{\mathbf{0}}_i \partial u^{\mathbf{g}}_j}\bigg|_{\text{eq}}, \tag{3}$$

where $\mathbf{0}$ labels the reference lattice cell, $\mathbf{g}$ identifies any direct space lattice vector within the SC, and $i, j = 1, \ldots, 3N$ are combined atomic and Cartesian indices that identify all possible Cartesian displacements $\mathbf{u}$ of the N atoms per cell. The Cartesian coordinates of all atoms in the reference cell in a given displaced configuration are represented by the vector $\mathbf{x} = \mathbf{x}^{\text{eq}} + \mathbf{u}^{\mathbf{0}}$, where $\mathbf{x}^{\text{eq}}$ are the equilibrium atomic positions.

A set of dynamical matrices $\mathbf{W}^{\mathbf{k}}$ is computed for a set of points within the first Brillouin zone—each labeled by a wave vector $\mathbf{k}$—via a Fourier transform of the mass-weighted interatomic force-constants of Eq. (3):

$$\mathbf{W}^{\mathbf{k}} = \sum_{\mathbf{g}\in SC} \mathbf{M}^{-\frac{1}{2}} \mathbf{H}^{\mathbf{g}} \mathbf{M}^{-\frac{1}{2}} e^{i\mathbf{k}\cdot\mathbf{g}}, \tag{4}$$

where $\mathbf{M}$ is the $3N \times 3N$ diagonal mass matrix, where the mass of each atom is repeated three times. Harmonic phonon frequencies and normal modes are obtained by diagonalization of the dynamical matrices of Eq. (4).

In this study, we are interested only in those lattice vibrations at the center of the first Brillouin zone (i.e., $\mathbf{k} = \mathbf{0}$ or Γ point) that are directly probed by infrared and Raman spectroscopies. Thus, we compute harmonic phonons at Γ from

$$\mathbf{C}^\dagger \mathbf{W}^\Gamma \mathbf{C} = \mathbf{\Lambda}^\Gamma, \tag{5}$$

where $\mathbf{\Lambda}^\Gamma$ is the $3N \times 3N$ eigenvalue matrix, and $\mathbf{C}$ is the adimensional $3N \times 3N$ eigenvector matrix, which contains the transformation coefficients from mass-weighted Cartesian to normal coordinates:

$$Q_\mu = \sum_i C_{i\mu} \sqrt{M_i}\, u_i, \tag{6}$$

where Q_μ labels a normal coordinate, with $\mu = 1, \ldots, 3N$. For three-dimensional (3D) periodic systems, the first three normal coordinates at Γ correspond to rigid translations along the three Cartesian directions. In the following, it proves convenient to introduce the mass-weighted form of the eigenvector matrix $\mathbf{C}$: $\tilde{\mathbf{L}} = \mathbf{M}^{-\frac{1}{2}}\mathbf{C}$, which is usually renormalized as follows:

$$\mathbf{L} = \frac{1}{(\tilde{\mathbf{L}}^\dagger \tilde{\mathbf{L}})^{\frac{1}{2}}} \tilde{\mathbf{L}} = \mathbf{M}_R^{\frac{1}{2}} \tilde{\mathbf{L}}, \tag{7}$$

where $\mathbf{M}_R$ is the $3N \times 3N$ diagonal matrix of normal mode reduced masses. The $\mathbf{L}$ matrix introduced in Eq. (7) satisfies the following relation:

$$\mathbf{L}^\dagger \mathbf{H^0} \mathbf{L} = \mathbf{K}, \tag{8}$$

i.e., it contains, arranged columnwise, the eigenvectors of the reference cell Hessian matrix $\mathbf{H^0}$, with eigenvalues in units of force constants arranged in the diagonal matrix $\mathbf{K}$.

LVMT [38,39], originally introduced by Konkoli and Cremer [55–59], is developed in terms of a set of internal coordinates q_n with $n = 1, \ldots, N_{\text{int}}$ (bond lengths, bond angles, dihedrals, puckering coordinates, etc.) where each q_n represents a distinct local vibration. The transformation matrix between Cartesian and internal coordinates is achieved via the Wilson $\mathbf{B}$ matrix, with elements [60,61]

$$B_{ni} = \frac{\partial q_n}{\partial u_i}. \tag{9}$$

The internal coordinates of the periodic system are defined via the redundant internal valence (RIV) approach [62–64] as implemented in the CRYSTAL electronic structure package [40,65] (i.e., $N_{\text{int}} \gg 3N$), instead of the well-known Z-matrix molecular approach, which poses several challenges when dealing with periodic systems [64,65]. The elements of Wilson's matrix in Eq. (9) are evaluated numerically through a two-sided finite-difference approach. The $\mathbf{L}$ and $\mathbf{B}$ transformation matrices can be combined to form a new transformation matrix between normal and internal coordinates:

$$\mathbf{D} = \mathbf{BL}, \tag{10}$$

where the $\mathbf{D}$ matrix has size $N_{\text{int}} \times 3N$ and where it proves convenient to identify its nth row vector as $\mathbf{d}_n$.

Within LVMT, a local vibrational mode vector $\mathbf{a}_n$ can be derived for each internal coordinate q_n [38,39]:

$$\mathbf{a}_n = \frac{\mathbf{K}^{-1}\mathbf{d}_n^\dagger}{\mathbf{d}_n \mathbf{K}^{-1} \mathbf{d}_n^\dagger}, \tag{11}$$

with an associated local force constant k_n^a, which can be used as an intrinsic indicator of bond, bending, and torsional strength [38,66]:

$$k_n^a = \mathbf{a}_n^\dagger \mathbf{K} \mathbf{a}_n = (\mathbf{d}_n \mathbf{K}^{-1} \mathbf{d}_n^\dagger)^{-1}. \tag{12}$$

The mass m_n^a associated with the local mode is obtained as

$$m_n^a = \frac{1}{\mathbf{B}_n \mathbf{M}^{-1} \mathbf{B}_n^\dagger}, \tag{13}$$

and the vibration frequency ω_n^a of the local mode as

$$\omega_n^a = \frac{1}{2\pi c} \sqrt{\frac{k_n^a}{m_n^a}}. \tag{14}$$

Additionally, the LVMT offers a framework to analyze delocalized normal modes in terms of local internal coordinates through the so-called characterization of normal modes (CNM) procedure [38,67–69]. Such a tool allows us to decompose a given normal mode, as described by its associated eigenvector $\mathbf{l}_\mu$ (i.e., the μth column of the $\mathbf{L}$ matrix), in terms of internal coordinate contributions. The contribution $S_{n\mu}$ of internal coordinate q_n to normal mode Q_μ is obtained as

$$S_{n\mu} = \frac{\langle \mathbf{a}_n^x | \mathbf{H^0} | \mathbf{l}_\mu \rangle^2}{\langle \mathbf{a}_n^x | \mathbf{H^0} | \mathbf{a}_n^x \rangle \langle \mathbf{l}_\mu | \mathbf{H^0} | \mathbf{l}_\mu \rangle}, \tag{15}$$

where $\mathbf{a}_n^x = \mathbf{L}\mathbf{a}_n$. The expression in Eq. (15) can be simplified in terms of previously defined quantities to (we report the demonstration in the ESI)

$$S_{n\mu} = \frac{D_{n\mu}^2 k_n^a}{K_{\mu\mu}}. \tag{16}$$

The contributions from the N_{int} internal coordinates to the μth normal mode are finally normalized and collected in the $\mathbf{\Xi}$ matrix with elements

$$\Xi_{n\mu} = \frac{S_{n\mu}}{\sum_m^{N_{\text{int}}} S_{m\mu}}. \tag{17}$$

We have implemented the LVMT outlined above in a developmental version of the CRYSTAL electronic structure package [40].

C. Thermal expansion

We compute the thermal expansion of the system through the quasiharmonic approximation (QHA) [70], where the Helmholtz free energy is obtained as

$$F^{\text{QHA}}(V,T) = E^{\text{el}}(V) + \frac{1}{2}\sum_i \hbar\omega_i(V) + k_B T \sum_i \left[\ln\left(1 - e^{-\frac{\hbar\omega_i(V)}{k_B T}}\right)\right], \tag{18}$$

where E^{el} is the static 0 K electronic internal energy of the crystal, the second term on the right-hand side (rhs) of Eq. (18)

is the zero-point energy, and ω_i are harmonic phonon frequencies. In the CRYSTAL package, harmonic phonon frequencies are computed at a few expanded/compressed volumes and individually fitted to quadratic polynomial functions [71–76]. The equilibrium volume at a given temperature, $V(T)$, can be obtained by minimizing the free energy in Eq. (18) with respect to the volume V, keeping T fixed. The volumetric thermal expansion coefficient is obtained as

$$\alpha_V(T) = \frac{1}{V(T)}\left(\frac{\partial V}{\partial T}\right)_p. \tag{19}$$

Analogous linear thermal expansion coefficients can be defined for individual lattice parameters [73,77,78].

D. Computational Details

All calculations reported in this work are performed with a developmental version of the CRYSTAL23 electronic structure package [40]. A global hybrid density functional approximation is used, namely PBE0 [79], as dispersion-corrected with Grimme's -D3 method [80], and as coupled with a triple-zeta basis set, POB-TZVP-rev2 [81]. The convergence in the self-consistent-field process is considered reached when the difference in energy between two consecutive cycles is below 10^{-9} Hartree. The truncation of the infinite Coulomb and exchange integral series is defined through the use of five different parameters, which are set here to 9 9 9 9 27 (see the TOLINTEG keyword in the Manual [82]). Numerical integration of the exchange-correlation potential is carried out using a pruned grid consisting of 300 radial point and 1454 angular ones. Reciprocal space is sampled over a $6 \times 6 \times 6$ Monkhorst-Pack grid within the first Brillouin zone, which corresponds to 80 symmetry independent **k**-points. The structure of $Mg(IO_3)_2$ has been optimized at 11 values of pressure in the range 0–10 GPa within the $P2_1$ space group via a hydrostatic constraint to the stress tensor [50,83]. Harmonic phonon frequencies (as well as IR and Raman spectra) and elastic stiffness constants are computed at each optimized structure. A topological analysis of the electron density is performed with the QTAIM as implemented in the TOPOND module [45,84–86].

III. RESULTS AND DISCUSSION

A. Structure and compressibility

To reliably describe the evolution with pressure of chemical bonding in $Mg(IO_3)_2$, we need to make sure to get a good description of its structural features. As recalled in the Introduction, Liang *et al.* [23] have performed XRD at different pressures, and they were able to determine the evolution with pressure of the lattice parameters of the monoclinic $P2_1$ phase (i.e., the length of the three lattice vectors **a**, **b**, **c**, the value of the β angle between **a** and **c**, and thus the volume V). Atomic positions within the cell could not be refined as a function of pressure. We report these experimental data in Fig. 2 as full circles. While the inspection of the evolution of the volume with pressure is not particularly telling—showing a regular overall compression—the analysis of individual lattice parameters is as follows: the structure is regularly compressed along the **b** lattice parameter as pressure increases, see Fig. 2(d), while it expands in the **ac** plane, only slightly so below 1 GPa of pressure and more pronouncedly so above 1 GPa, see Fig. 2(c). The structural parameters obtained from our simulations are reported as solid lines in the same plots. Apart from a slight overall underestimation of the volume (to be expected, as the experiments were performed at room temperature while thermal expansion is not accounted for in our simulations), all trends upon compression are well reproduced. This is particularly remarkable for the **a** and **c** lattice parameters, which are key in the description of the observed phonon softening. Indeed, inspection of Figs. 1(a) and 1(b) shows how the three strong I-O_{fn} bonds within IO_3 units are mainly oriented in the **ac** crystallographic plane. The expansion of the lattice upon compression in the **ac** plane is intrinsically linked to the elongation of the I-O_{fn} bonds. Let us note in passing that previous simulations were not able to describe this subtle structural feature (dotted lines in Fig. 2) [23] probably because of missing dispersive, van der Waals, interactions, as documented in Fig. S1 of the Supplemental Material (SM) [87]. At the same time, inspection of Fig. 1(b) shows schematically how the LEPs of iodine atoms are mainly oriented along the **b** crystallographic axis, as are the I-O_{sn} interactions to which they contribute. These weaker interactions are easily compressed, which results in the contraction of the **b** axis shown in Fig. 2(d). We report the evolution of the β lattice angle in Fig. 2(e), which is also well reproduced by the present simulations. Let us note that it regularly converges to the value of 120° as the monoclinic $P2_1$ to trigonal $P3$ phase transition approaches.

We report the evolution with pressure of individual I-O bond lengths in Fig. 2(f). While a direct comparison with the experiment is not possible, as atomic positions under compression could not be refined from XRD, we expect these reported trends to be reliable based on the remarkable agreement on all lattice parameters discussed above. The three weak I-O_{sn} interactions (magenta solid lines at the top) decrease with pressure with a trend that closely follows the one previously discussed on the **b** crystallographic axis. The three strong I-O_{fn} interactions (violet solid lines at the bottom) instead elongate with pressure with a quasilinear trend. In Sec. III B, we will show how this elongation is reflected in phonon softening and redshifting of specific bands in the IR and Raman spectra of the material. In Fig. 2(g), we report the evolution with pressure of the six Mg-O bond lengths within the MgO_6 octahedral distorted units: at low pressure the distortion is more pronounced, with the six bond lengths being distinct, while it decreases with pressure when approaching the phase transition, with two pairs of equivalent bonds being formed.

Let us inspect more closely the low pressure region, where experimental data show a discontinuity in the slope of the **a**, **b,** and β lattice parameters at about 1.5 GPa. Although not as pronounced as in the experimental data, our simulations do capture a subtle change in the slope of these lattice parameters at about 2 GPa. Interestingly, a phase transition in that pressure range has been suggested to occur in two isostructural materials: $Co(IO_3)_2$ at about 3 GPa [88], and $Zn(IO_3)_2$ at about 2.5-3.4 GPa [31]. In both cases, an isostructural phase transition was suggested (i.e., a transition between two phases belonging to the same space group of symmetry, $P2_1 \rightarrow P2_1$)

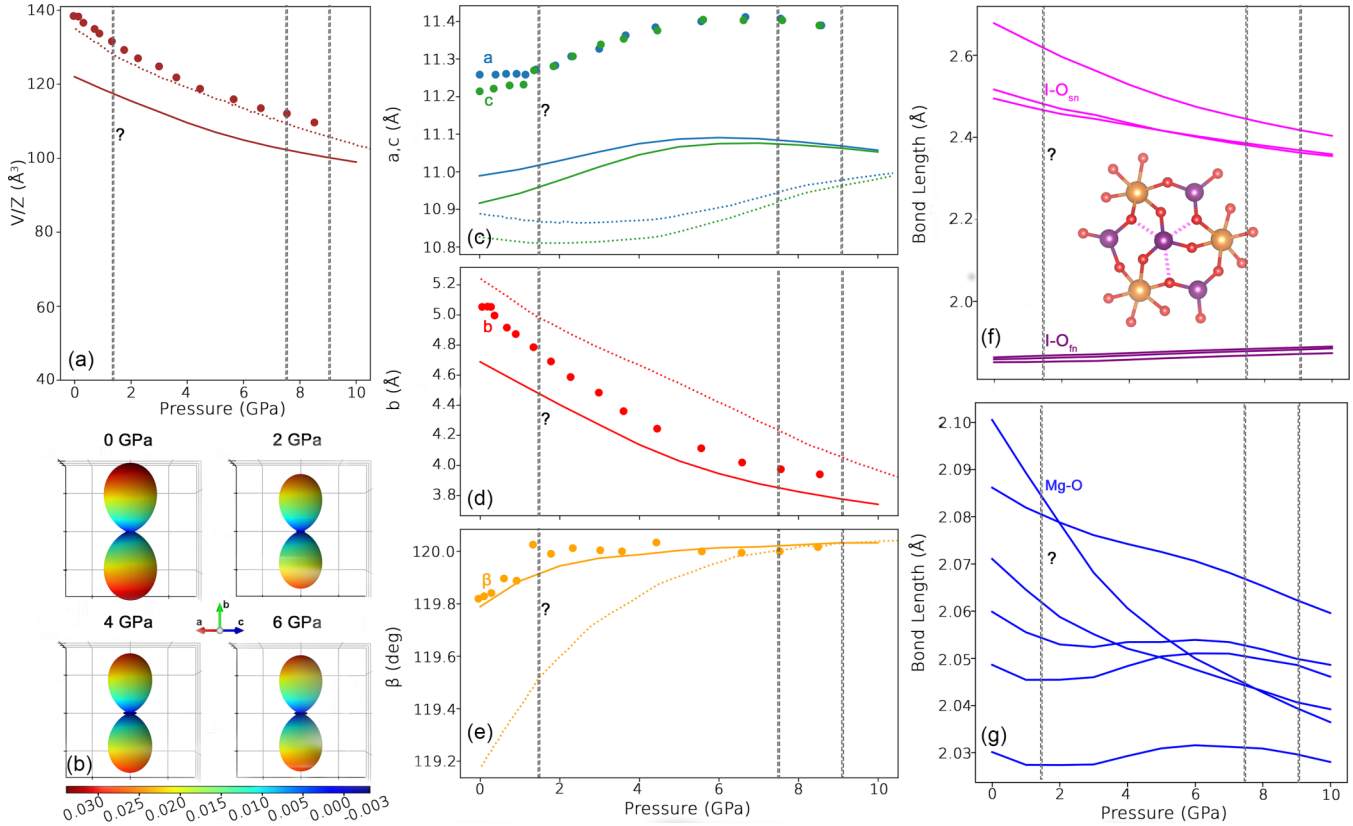

FIG. 2. Evolution with pressure of the structure and mechanical response of $Mg(IO_3)_2$. Results from present calculations (solid lines) are compared with experimental data (full circles) and previous simulations (dotted lines) from Ref. [23]. (a) Volume (per formula unit); (b) 3D plots of the linear compressibility β (in GPa^{-1}); (c) lattice vectors **a** (blue) and **c** (green); (d) lattice vector **b**; (e) lattice angle β; (f) bond lengths of $I\text{-}O_{fn}$ and $I\text{-}O_{sn}$ interactions; (g) bond length of Mg-O interactions in the distorted MgO_6 octahedral unit. In all panels, vertical dashed lines at 7.5 and 9.7 GPa mark the experimental transition pressure range from the monoclinic $P2_1$ to the trigonal $P3$ phase. Dashed vertical lines at 1.5 GPa mark the hypothetical $P2_1 \rightarrow P2_1$ phase transition and are labeled with a "?".

primarily based on the observed discontinuity (i.e., change in slope) of various structural parameters on pressure. In particular, we note that our simulated trends are qualitatively very similar to those previously reported for $Co(IO_3)_2$ [88]. Thus, although it is difficult to draw definitive conclusions, our simulated data would be consistent with an isostructural $P2_1 \rightarrow P2_1$ phase transition occurring at about 1.5–2 GPa in $Mg(IO_3)_2$.

We analyze the evolution with pressure of the mechanical response of $Mg(IO_3)_2$ in Fig. 2(b), where we report 3D plots of the linear compressibility β defined in Eq. (2) at four pressures (0, 2, 4, and 6 GPa). At zero pressure, the system is clearly characterized by a strong anisotropy in the elastic response with a large positive linear compressibility along the **b** crystallographic axis and a small and negative linear compressibility in the **ac** crystallographic plane. As pressure increases, two effects are observed: (i) a decrease in $|\beta|$ along the **b** axis; and (ii) an increase in $|\beta|$ in the **ac** plane (i.e., more negative linear compressibility values).

Many materials exhibiting negative linear compressibility are also characterized by a negative thermal expansion [32–37]. In Fig. 3, we investigate the thermal expansion of $Mg(IO_3)_2$, as obtained from a quasiharmonic treatment described in Sec. II C, where harmonic phonon frequencies were computed at four volumes from a –2% compression to a

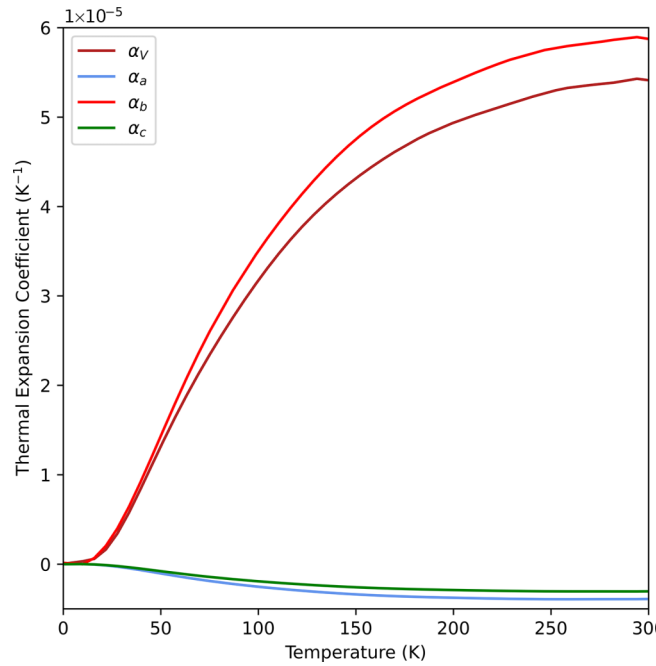

FIG. 3. Thermal expansion coefficients of $Mg(IO_3)_2$ computed within the quasiharmonic approximation.

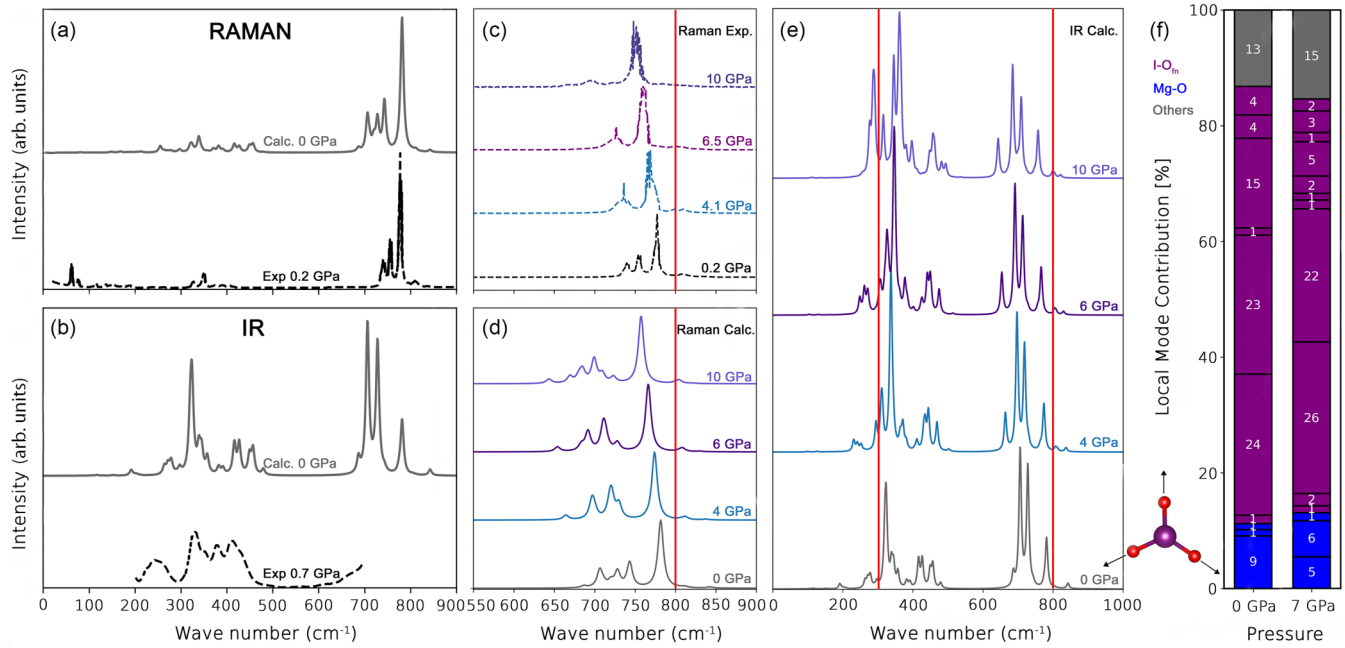

FIG. 4. Phonon softening in $Mg(IO_3)_2$. (a) Simulated Raman spectrum at zero pressure and experimental spectrum at 0.2 GPa from Ref. [23]; (b) simulated IR spectrum at zero pressure and experimental spectrum at 0.7 GPa from Ref. [23]; (c),(d) evolution with pressure of the I-O stretching region of the Raman spectrum from theory (this study) and experiments from Ref. [23]; (e) evolution with pressure of the computed IR spectrum; (f) decomposition of the symmetric stretching mode of IO_3 units (i.e., the most intense feature in the Raman spectrum) in terms of internal, localized coordinates at 0 and 7 GPa. Vertical red lines are only to guide the eye.

+4% expansion. As expected based on the structural analysis discussed above, the thermal expansion of this system is found to be strongly anisotropic. In particular, $Mg(IO_3)_2$ exhibits a large positive thermal expansion along the **b** lattice parameter (red solid line in the figure) and a smaller and negative thermal expansion in the **ac** plane (blue and green solid lines in the figure for α_a and α_c linear thermal expansion coefficients, respectively). The overall volumetric thermal expansion coefficient of the system, α_V, is positive, with a value of about 5×10^{-5} K^{-1} at 300 K.

B. Infrared and Raman spectra

We now analyze how the pressure-induced structural changes discussed above are reflected on IR and Raman vibrational spectra of $Mg(IO_3)_2$. The interatomic force constants in Eq. (3) are in general very sensitive to subtle features of the potential energy surface (PES) and thus to subtle changes in the interatomic interactions. We have computed IR and Raman spectra of $Mg(IO_3)_2$ as a function of pressure following a computational strategy outlined in Ref. [89]. Let us note that, within the symmetry constraints of the $P2_1$ space group, none of the harmonic phonon frequencies at the Γ point become imaginary up to 10 GPa of pressure. We report our simulated spectra at zero pressure in Figs. 4(a) and 4(b), where they are compared with experimental spectra from Ref. [23] at the lowest available pressure (0.7 GPa for the IR spectrum and 0.2 GPa for the Raman spectrum). The agreement with the experiment is satisfactory. The following can be observed: (i) main peak positions in the Raman spectrum are predicted with good accuracy in the whole 0−1000 cm^{-1} range; (ii) the experimental IR spectrum was recorded only up to 700 cm^{-1} and thus lacks the main peaks associated with I-O stretching motions, which we report in the simulated spectrum; (iii) the simulated IR spectrum in the 200−500 cm^{-1} range is slightly redshifted relative to the experimental one, which is consistent with the experiment being performed at 0.7 GPa (see below for a detailed description of the pressure evolution of the spectra). Let us analyze the Raman spectrum more closely. Two main regions can be identified in the spectrum, one located between 200 and 500 cm^{-1}, associated with bending modes within the iodate IO_3 unit, and the other located between 600 and 800 cm^{-1}, associated with I-O stretching motions characterized by the most intense features. The most prominent feature in the first spectral region is found at ∼340 cm^{-1} and corresponds to the scissoring of the iodate unit, with smaller peaks at ∼380 and 420 cm^{-1}. As pressure is applied to the system, all peaks in this region are blueshifted. The I-O stretching region exhibits the most intense feature at 781 cm^{-1}, which can be assigned to the symmetric stretching motion within the IO_3 unit, with lower intensity features at ∼705, 730, 740, and a shoulder peak at ∼690 cm^{-1}, which can all be assigned to distinct asymmetric stretching motions. This region follows a more uncommon behavior upon compression, as highlighted in Figs. 4(c) and 4(d). Indeed, as pressure increases, all peaks in this region get redshifted, suggesting the weakening of the corresponding $I\text{-}O_{fn}$ interactions. Our simulations predict a softening rate with pressure that closely matches the experiment. We visually inspect the normal modes of selected spectral features in the O–I–O bending and I–O stretching region in Fig. S2 of the SM. In stretching vibrations, the atoms are displaced along the $I\text{–}O_{fn}$ axes, which are mainly oriented in the **ac** crystallographic plane, which is expanding upon compression, thus yielding a redshift

TABLE I. Quantitative characterization of I–O interactions in $Mg(IO_3)_2$ as a function of pressure from the LVMT and the QTAIM. Adiabatic local force constant k^a (mdyn/Å), distance of bond CP from oxygen and iodine atoms (Å)—the relative position of the CP along the I–O path is given within parentheses (%), electron density at the bond CP ρ (a.u.), Laplacian of the electron density at the bond CP $\nabla^2\rho$ (a.u.), "bond degree" index H/ρ (a.u.), ratio between the potential energy density V and the kinetic energy density G at the bond CP, $|V|/G$.

Bond	Pressure	k^a	$d_{\text{CP-O}}$	$d_{\text{CP-I}}$	ρ	$\nabla^2\rho$	H/ρ	$\lvert V\rvert/G$
	0	4.245	0.909 (48.90)	0.950 (51.10)	0.173	0.376	–0.592	1.521
	2	4.099	0.912 (48.95)	0.951 (51.05)	0.172	0.368	–0.590	1.524
$I–O_{fn}$	4	3.934	0.915 (48.98)	0.953 (51.02)	0.170	0.360	–0.586	1.526
	6	3.748	0.918 (48.99)	0.956 (51.01)	0.168	0.350	–0.582	1.528
	8	3.611	0.922 (49.04)	0.958 (50.96)	0.166	0.343	–0.578	1.529
	10	3.471	0.924 (49.04)	0.960 (50.96)	0.165	0.337	–0.576	1.530
	0	0.492	1.221 (45.54)	1.460 (54.46)	0.032	0.094	–0.027	1.036
	2	0.604	1.192 (45.85)	1.408 (54.15)	0.038	0.105	–0.066	1.088
$I–O_{sn}$	4	0.680	1.169 (46.17)	1.363 (53.83)	0.043	0.113	–0.102	1.135
	6	0.760	1.150 (46.41)	1.328 (53.59)	0.048	0.120	–0.133	1.177
	8	0.825	1.137 (46.62)	1.302 (53.38)	0.052	0.125	–0.157	1.209
	10	0.876	1.126 (46.78)	1.281 (53.22)	0.056	0.129	–0.177	1.235

in the 700−800 cm^{-1} region. In bending vibrations, instead, the atoms are displaced mainly along the **b** crystallographic axis, which is compressing upon pressure, thus consistently yielding a blueshift in the 200−500 cm^{-1} region. The LVMT outlined in Sec. II B allows us to decompose normal modes of vibration in terms of internal, localized coordinates; see Eq. (15). Figure 4(f) reports such a decomposition at two pressures (0 and 7 GPa) for the vibration mode responsible for the most intense feature in the Raman spectrum of $Mg(IO_3)_2$, that is, the symmetric stretching of the IO_3 units. Contributions from $I–O_{fn}$ and Mg–O bond lengths are reported in violet and blue, respectively (other contributions smaller than 1% are grouped in gray). As pressure increases and $I–O_{fn}$ bonds elongate and weaken, this symmetric stretching vibration becomes less localized just on the IO_3 unit. We analyze the THz region of the Raman spectrum in Fig. S3 of the SM and in the associated discussion, where the effect of temperature and laser frequency are explicitly analyzed [90,91]. The overall picture emerging from the analysis of the Raman spectra is confirmed by the evolution with pressure of the IR spectrum. We report simulated IR spectra as a function of pressure in Fig. 4(e). Peaks in the 200−500 cm^{-1} bending region are consistently blueshifted by pressure. In terms of the shape of the spectral profile, the most notable change is represented by the rise in intensity of the peaks below 300 cm^{-1}, particularly so for the feature at 264 cm^{-1} at zero pressure, which corresponds to a rocking motion in the iodate unit. The I-O stretching region is instead redshifted by pressure, which is again consistent with what is observed in the Raman spectrum and on the structural parameters.

C. I–O bond strength

We shall now complement the qualitative picture outlined above with two distinct quantitative approaches to assess the strength of the I-O interactions in $Mg(IO_3)_2$ and their evolution with pressure: the LVMT described in Sec. II B, as extended to periodic systems in this study, and the well-known QTAIM. These two theories allow us to estimate the strength of certain chemical interactions in two very distinct ways: through the dynamics of vibrational motions and interatomic force constants, and through the topology of the static electron density, respectively. Results from both approaches are summarized in Table I for one $I–O_{fn}$ and one $I–O_{sn}$ interaction. The key bond strength indicator from the LVMT is represented by the adiabatic local force constant k^a given in Eq. (12), specific to the internal coordinate that corresponds to the length of the target bond. This quantity is reported in the table at six different pressures in the range 0–10 GPa. The local force constant of the short $I–O_{fn}$ interaction decreases with pressure, describing the weakening of the interaction upon compression. Passing from 0 to 10 GPa, the force constant decreases from 4.245 to 3.471 mdyn/Å (i.e., a decrease of 18%). Conversely, the force constant of the long $I–O_{sn}$ interaction increases with pressure, describing the strengthening of this interaction upon compression. Passing from 0 to 10 GPa, the force constant increases from 0.492 to 0.876 mdyn/Å (i.e., an increase of 78%). These trends are confirmed by the QTAIM, which also allows for one further important clarification. In their seminal study, Liang *et al.* [23] suggested the formation of new I-O bonds upon compression. A thorough topological analysis of the electron density of the system shows that the $I–O_{sn}$ chemical bonds are already present at zero pressure. Within the QTAIM, the existence of a chemical bond is determined by the presence of an associated bond critical point (CP) of the electron density. The type of chemical interaction is classified based on the local value at the CP of a few indicators: the electron density ρ, the Laplacian of the electron density $\nabla^2\rho$, various energy densities, and combinations thereof. Bond CPs are found along each $I–O_{fn}$ and $I–O_{sn}$ interaction, with parameters reported in Table I. Both interactions are of mixed ionic-covalent character, with a positive Laplacian of the density $\nabla^2\rho > 0$, a negative total energy density $H < 0$, and the ratio between the potential and kinetic energy density between 1 and 2, $1 < |V|/G < 2$. As pressure increases, the bond CP of the $I–O_{fn}$ interaction moves toward the iodine atom, the density at the bond CP decreases, as does the "bond degree" index H/ρ. Conversely, the electron density at the bond CP of the $I–O_{sn}$ interaction

increases upon compression along with the absolute value of the "bond degree" index.

IV. CONCLUSIONS

We have investigated the evolution under pressure of several properties (structure, elasticity, lattice dynamics, infrared and Raman spectra, bonding) of the monoclinic $P2_1$ phase of $Mg(IO_3)_2$ with density functional theory (DFT) simulations by use of a global hybrid density functional approximation.

As pressure increases, three I–O interactions within $[IO_3]$ structural units weaken and elongate, which results in (i) the phonon softening of certain bands assigned to I-O stretching modes (observed in infrared and Raman spectra); (ii) the expansion of the **a** and **c** lattice vectors, which translates into a negative linear compressibility (NLC) in the **ac** plane. This is accompanied by the shortening and strengthening of the interaction of iodine atoms with their three second-neighboring oxygen atoms, with a corresponding compression of the **b** lattice vector along which they are mainly oriented.

The strength of various interatomic interactions, as well as their evolution with pressure, is assessed in terms of local mode adiabatic force constants obtained through a new periodic implementation of the local vibrational mode theory (LVMT).

ACKNOWLEDGMENTS

We thank SMU's O'Donnell Data Science and Research Computing Institute for providing excellent computational resources. F.B. thanks SMU's Moody School of Graduate and Advanced Studies for a Dissertation fellowship. This research has received funding from the Project CH4.0 under the MUR program "Dipartimenti di Eccellenza 2023-2027" (CUP: D13C22003520001).

DATA AVAILABILITY

The data that support the findings of this article are not publicly available upon publication because it is not technically feasible and/or the cost of preparing, depositing, and hosting the data would be prohibitive within the terms of this research project. The data are available from the authors upon reasonable request.

[1] H.-Y. Chang, S.-H. Kim, K. M. Ok, and P. S. Halasyamani, Polar or nonpolar? A^+ cation polarity control in $A_2Ti(IO_3)_6$ (A = Li, Na, K, Rb, Cs, Tl), J. Am. Chem. Soc. **131**, 6865 (2009).

[2] H.-Y. Chang, S.-H. Kim, P. S. Halasyamani, and K. M. Ok, Alignment of lone pairs in a new polar material: Synthesis, characterization, and functional properties of $Li_2Ti(IO_3)_6$, J. Am. Chem. Soc. **131**, 2426 (2009).

[3] A. Liang, R. Turnbull, P. Rodríguez-Hernandez, A. Muñoz, M. Jasmin, L.-T. Shi, and D. Errandonea, General relationship between the band-gap energy and iodine-oxygen bond distance in metal iodates, Phys. Rev. Mater. **6**, 044603 (2022).

[4] A. Liang, R. Turnbull, and D. Errandonea, A review on the advancements in the characterization of the high-pressure properties of iodates, Prog. Mater. Sci. **136**, 101092 (2023).

[5] C. Sun, B. Yang, and J. Mao, Structures and properties of functional metal iodates, Sci. China Chem. **54**, 911 (2011).

[6] C.-F. Sun, C.-L. Hu, X. Xu, J.-B. Ling, T. Hu, F. Kong, X.-F. Long, and J.-G. Mao, $BaNbO(IO_3)_5$: A new polar material with a very large SHG response, J. Am. Chem. Soc. **131**, 9486 (2009).

[7] S. D. Nguyen, J. Yeon, S.-H. Kim, and P. S. Halasyamani, $BiO(IO_3)$: A new polar iodate that exhibits an aurivillius-type $(Bi_2O_2)2^+$ layer and a large SHG response, J. Am. Chem. Soc. **133**, 12422 (2011).

[8] X. Xu, C.-L. Hu, B.-X. Li, B.-P. Yang, and J.-G. Mao, α-AgI_3O_8 and β-AgI_3O_8 with large SHG responses: Polymerization of IO_3 groups into the I_3O_8 polyiodate anion, Chem. Mater. **26**, 3219 (2014).

[9] Y. Huang, X. Meng, P. Gong, L. Yang, Z. Lin, X. Chen, and J. Qin, $A_2BiI_5O_{15}$ ($A = K^+$ Or Rb^+): Two new promising nonlinear optical materials containing $[I_3O_9]3^-$ bridging anionic groups, J. Mater. Chem. C **2**, 4057 (2014).

[10] L. Xiao, Z. Cao, J. Yao, Z. Lin, and Z. Hu, A new Cerium iodate infrared nonlinear optical material with a large second-harmonic generation response, J. Mater. Chem. C **5**, 2130 (2017).

[11] F.-F. Mao, C.-L. Hu, J. Chen, B.-L. Wu, and J.-G. Mao, $HBa_{2.5}(IO_3)_6(I_2O_5)$ and $HBa(IO_3)(I4O_{11})$: Explorations of second-order nonlinear optical materials in the alkali-earth polyiodate system, Inorg. Chem. **58**, 3982 (2019).

[12] C.-L. Hu and J.-G. Mao, Recent advances on second-order NLO materials based on metal iodates, Coord. Chem. Rev. **288**, 1 (2015).

[13] D. Phanon, B. Bentria, D. Benbertal, A. Mosset, and I. Gautier-Luneau, New potential materials for infrared nonlinear optics. Preparation, characterisation and optical transparency of monometallic and bimetallic iodates, Solid State Sci. **8**, 1466 (2006).

[14] D. Phanon, A. Mosset, and I. Gautier-Luneau, New materials for infrared non-linear optics. Syntheses, structural characterisations, second harmonic generation and optical transparency of $M(IO_3)_3$ metallic iodates, J. Mater. Chem. **17**, 1123 (2007).

[15] D. Phanon and I. Gautier-Luneau, Promising material for infrared nonlinear optics: NaI_3O_8 salt containing an octaoxotriiodate (V) anion formed from condensation of $[IO_3]^-$ ions, Ang. Chem. Int. Ed. **46**, 8488 (2007).

[16] A. Liang, S. Rahman, P. Rodriguez-Hernandez, A. Muñoz, F. J. Manjón, G. Nenert, and D. Errandonea, High-Pressure raman study of $Fe(IO_3)_3$: Soft-Mode behavior driven by coordination changes of iodine atoms, J. Phys. Chem. C **124**, 21329 (2020).

[17] H. Fan, G. Peng, C. Lin, K. Chen, S. Yang, and N. Ye, $Ba(IO_3)F$: An alkaline-earth-metal iodate fluoride crystal with large band gap and birefringence, Inorg. Chem. **59**, 7376 (2020).

[18] H. Jo, H. G. Kim, H. R. Byun, J. I. Jang, and K. M. Ok, Synthesis, structure, and third-harmonic generation measurements of

a mixed alkali metal iodate, $KLi_2(IO_3)_3$, J. Solid State Chem. **282**, 121120 (2020).

[19] H. Liu, X. Jiang, X. Wang, L. Yang, Z. Lin, Z. Hu, X. Meng, X. Chen, and J. Qin, Influence of a-site cations on Germanium iodates as mid-IR nonlinear optical materials: $A_2Ge(IO_3)_6$ (A = Li, K, Rb and Cs) and bage $(IO_3)_6$ H_2O, J. Mater. Chem. C **6**, 4698 (2018).

[20] K. M. Ok and P. S. Halasyamani, New metal iodates: Syntheses, structures, and characterizations of noncentrosymmetric $La(IO_3)_3$ and $NaYI_4O_{12}$ and centrosymmetric β-$Cs_2I_4O_{11}$ and $Rb_2I_6O_{15}(OH)_2 \cdot H_2O$, Inorg. Chem. **44**, 9353 (2005).

[21] L. Lin, L. Li, C. Wu, Z. Huang, M. G. Humphrey, and C. Zhang, Incorporating rare-earth cations with moderate electropositivity into iodates for the optimized second-order nonlinear optical performance, Inorg. Chem. Front. **7**, 2736 (2020).

[22] A. Liang, L.-T. Shi, R. Turnbull, F. J. Manjón, J. Ibáñez, C. Popescu, M. Jasmin, J. Singh, K. Venkatakrishnan, G. Vaitheeswaran, *et al.*, Pressure-Induced band-gap energy increase in a metal iodate, Phys. Rev. B **106**, 235203 (2022).

[23] A. Liang, R. Turnbull, C. Popescu, F.-J. Manjón, E. Bandiello, P. Rodriguez-Hernandez, A. Muñoz, I. Yousef, Z. Hebboul, and D. Errandonea, Pressure-Induced phase transition and increase of oxygen-iodine coordination in Magnesium iodate, Phys. Rev. B **105**, 054105 (2022).

[24] Y.-L. Deng, C.-L. Hu, X. Xu, M.-Z. Zhang, and J.-G. Mao, $Na[B_3IO_7(OH)]$ and $Na_2[B_4IO_9](IO_3)$: Explorations of boroiodates with strong second harmonic generation response and large birefringence, J. Am. Chem. Soc. **147**, 12858 (2025).

[25] M.-Q. Lin, C.-L. Hu, M.-F. Duan, B.-X. Li, J.-G. Mao, and B.-P. Yang, Potassium Tetraiodatoiodate (III) iodate (V): A nonlinear optical crystal with exceptional second-harmonic generation and full-wavelength phase matching, Ang. Chem. Int. Ed. **64**, e202504673 (2025).

[26] V. Oliveira, E. Kraka, and D. Cremer, The intrinsic strength of the halogen bond: Electrostatic and covalent contributions described by coupled cluster theory, Phys. Chem. Chem. Phys. **18**, 33031 (2016).

[27] V. P. Oliveira, B. L. Marcial, F. B. C. Machado, and E. Kraka, Metal-halogen bonding seen through the eyes of vibrational spectroscopy, Materials **13**, 55 (2020).

[28] Y. Tao, Y. Qiu, W. Zou, S. Nanayakkara, S. Yannacone, and E. Kraka, *In situ* assessment of intrinsic strength of X-I $\cdots$ OA type halogen bonds in molecular crystals with periodic local vibrational mode theory, Molecules **25**, 1589 (2020).

[29] M. Freindorf, S. Yannacone, V. Oliveira, N. Verma, and E. Kraka, Halogen bonding involving I_2 and d^8 transition-metal pincer complexes, Crystals **11**, 373 (2021).

[30] K. Bu, H. Luo, S. Guo, M. Li, D. Wang, H. Dong, Y. Ding, W. Yang, and X. Lü, Pressure-Regulated dynamic stereochemical role of lone-pair electrons in layered Bi_2O_2S, J. Phys. Chem. Lett. **11**, 9702 (2020).

[31] A. Liang, C. Popescu, F.-J. Manjón, P. Rodriguez-Hernandez, A. Muñoz, Z. Hebboul, and D. Errandonea, Structural and vibrational study of $Zn(IO_3)_2$ combining high-pressure experiments and density-functional theory, Phys. Rev. B **103**, 054102 (2021).

[32] A. L. Goodwin, M. Calleja, M. J. Conterio, M. T. Dove, J. S. Evans, D. A. Keen, L. Peters, and M. G. Tucker, Colossal positive and negative thermal expansion in the framework material $Ag_3[Co(CN)_6]$, Science **319**, 794 (2008).

[33] A. L. Goodwin, D. A. Keen, and M. G. Tucker, Large negative linear compressibility of $Ag_3[Co(CN)_6]$, Proc. Natl. Acad. Sci. USA **105**, 18708 (2008).

[34] M. K. Gupta, B. Singh, R. Mittal, M. Zbiri, A. B. Cairns, A. L. Goodwin, H. Schober, and S. L. Chaplot, Anomalous thermal expansion, negative linear compressibility, and high-pressure phase transition in $ZnAu_2(CN)_4$: Neutron inelastic scattering and lattice dynamics studies, Phys. Rev. B **96**, 214303 (2017).

[35] B. Singh, M. K. Gupta, R. Mittal, M. Zbiri, T. R. Ravindran, H. Schober, and S. L. Chaplot, Phonons and anomalous lattice behavior in $KMnAg_3(CN)_6$ and $KNiAu_3(CN)_6$: Inelastic neutron scattering and first-principles calculations, J. Phys. Chem. C **124**, 7216 (2020).

[36] M. R. Ryder, J. Maul, B. Civalleri, and A. Erba, Quasi-harmonic lattice dynamics of a prototypical metal–organic framework, Adv. Theor. Simul. **2**, 1900093 (2019).

[37] J. Linnera, A. Erba, and A. J. Karttunen, Negative thermal expansion of Cu_2O studied by quasi-harmonic approximation and cubic force-constant method, J. Chem. Phys. **151**, 184109 (2019).

[38] E. Kraka, M. Quintano, H. W. La Force, J. J. Antonio, and M. Freindorf, The local vibrational mode theory and its place in the vibrational spectroscopy arena, J. Phys. Chem. A **126**, 8781 (2022).

[39] E. Kraka, W. Zou, and Y. Tao, Decoding chemical information from vibrational spectroscopy data: Local vibrational mode theory, WIREs Comput. Mol. Sci. **10**, e1480 (2020).

[40] A. Erba, J. K. Desmarais, S. Casassa, B. Civalleri, L. Donná, I. J. Bush, B. Searle, L. Maschio, L. Edith-Daga, A. Cossard, C. Ribaldone, E. Ascrizzi, N. L. Marana, J.-P. Flament, and B. Kirtman, CRYSTAL23: A program for computational solid state physics and chemistry, J. Chem. Theor. Comput. **19**, 6891 (2023).

[41] W. Zou, Y. Tao, M. Freindorf, D. Cremer, and E. Kraka, Local vibrational force constants - from the assessment of empirical force constants to the description of bonding in large systems, Chem. Phys. Lett. **748**, 137337 (2020).

[42] S. Nanayakkara, Y. Tao, and E. Kraka, Capturing individual Hydrogen bond strengths in ices via periodic local vibrational mode theory: Beyond the lattice energy picture, J. Chem. Theor. Comput. **18**, 562 (2022).

[43] F. Bodo, A. Erba, E. Kraka, and R. T. Moura, Jr., Chemical bonding in uranium-based materials: A local vibrational mode case study of $Cs_2UO_2Cl_4$ and UCl_4 crystals, J. Comput. Chem. **45**, 1130 (2024).

[44] R. F. Bader, Atoms in molecules, Acc. Chem. Res. **18**, 9 (1985).

[45] C. Gatti, V. Saunders, and C. Roetti, Crystal field effects on the topological properties of the electron density in molecular crystals: The case of urea, J. Chem. Phys. **101**, 10686 (1994).

[46] J. F. Nye, *et al.*, *Physical Properties of Crystals: Their Representation by Tensors and Matrices* (Oxford University Press, Oxford, UK, 1985).

[47] W. F. Perger, J. Criswell, B. Civalleri, and R. Dovesi, *Ab-initio* calculation of elastic constants of crystalline systems with the crystal code, Comput. Phys. Commun. **180**, 1753 (2009).

[48] A. Erba, A. Mahmoud, R. Orlando, and R. Dovesi, Elastic properties of six silicate garnet end-members from accurate *ab initio* simulations, Phys. Chem. Miner. **41**, 151 (2014).

[49] A. Erba, D. Caglioti, C. M. Zicovich-Wilson, and R. Dovesi, Nuclear-relaxed elastic and piezoelectric constants of materials:

Computational aspects of two quantum-mechanical approaches, J. Comput. Chem. **38**, 257 (2017).

[50] A. Erba, A. Mahmoud, D. Belmonte, and R. Dovesi, High pressure elastic properties of minerals from *ab initio* simulations: The case of pyrope, grossular and andradite silicate garnets, J. Chem. Phys. **140**, 124703 (2014).

[51] M. Destefanis, C. Ravoux, A. Cossard, and A. Erba, Thermo-Elasticity of materials from quasi-harmonic calculations, Minerals **9**, 16 (2019).

[52] R. E. Newnham, *Properties of Materials: Anisotropy, Symmetry, Structure* (Oxford University Press on Demand, Oxford, UK, 2005).

[53] B. Camino, H. Zhou, E. Ascrizzi, A. Boccuni, F. Bodo, A. Cossard, D. Mitoli, A. M. Ferrari, A. Erba, and N. M. Harrison, Crystalpytools: A python infrastructure for the crystal code, Comput. Phys. Commun. **292**, 108853 (2023).

[54] J. Baima, M. Ferrabone, R. Orlando, A. Erba, and R. Dovesi, Thermodynamics and phonon dispersion of pyrope and grossular silicate garnets from *ab initio* simulations, Phys. Chem. Miner. **43**, 137 (2016).

[55] Z. Konkoli and D. Cremer, A new way of analyzing vibrational spectra. I. Derivation of adiabatic internal modes, Int. J. Quantum Chem. **67**, 1 (1998).

[56] Z. Konkoli, J. A. Larsson, and D. Cremer, A new way of analyzing vibrational spectra. II. Comparison of internal mode frequencies, Int. J. Quantum Chem. **67**, 11 (1998).

[57] Z. Konkoli and D. Cremer, A new way of analyzing vibrational spectra. III. Characterization of normal vibrational modes in terms of internal vibrational modes, Int. J. Quantum Chem. **67**, 29 (1998).

[58] Z. Konkoli, J. A. Larsson, and D. Cremer, A new way of analyzing vibrational spectra. IV. Application and testing of adiabatic modes within the concept of the characterization of normal modes, Int. J. Quantum Chem. **67**, 41 (1998).

[59] D. Cremer, J. A. Larsson, and E. Kraka, in *Theoretical and Computational Chemistry*, edited by C. Parkanyi (Elsevier, Amsterdam, 1998), pp. 259–327.

[60] E. B. Wilson, J. C. Decius, and P. C. Cross, *Molecular Vibrations: The Theory of Infrared and Raman Vibrational Spectra* (Courier, Mineola, NY, 1980).

[61] V. Bakken and T. Helgaker, The efficient optimization of molecular geometries using redundant internal coordinates, J. Chem. Phys. **117**, 9160 (2002).

[62] P. Pulay and G. Fogarasi, Geometry optimization in redundant internal coordinates, J. Chem. Phys. **96**, 2856 (1992).

[63] C. Peng, P. Y. Ayala, H. B. Schlegel, and M. J. Frisch, Using redundant internal coordinates to optimize equilibrium geometries and transition states, J. Comput. Chem. **17**, 49 (1996).

[64] K. N. Kudin, G. E. Scuseria, and H. B. Schlegel, A redundant internal coordinate algorithm for optimization of periodic systems, J. Chem. Phys. **114**, 2919 (2001).

[65] A. Rimola, C. M. Zicovich-Wilson, R. Dovesi, and P. Ugliengo, Search and characterization of transition state structures in crystalline systems using valence coordinates, J. Chem. Theor. Comput. **6**, 1341 (2010).

[66] W. Zou and D. Cremer, C_2 in a box: Determining its intrinsic bond strength for the $X^1\Sigma_g^+$ ground state, Chem. Eur. J. **22**, 4087 (2016).

[67] Y. Tao, C. Tian, N. Verma, W. Zou, C. Wang, D. Cremer, and E. Kraka, Recovering intrinsic fragmental vibrations using the generalized subsystem vibrational analysis, J. Chem. Theor. Comput. **14**, 2558 (2018).

[68] N. Verma, Y. Tao, W. Zou, X. Chen, X. Chen, M. Freindorf, and E. Kraka, A critical evaluation of vibrational stark effect (VSE) probes with the local vibrational mode theory, Sensors **20**, 2358 (2020).

[69] R. T. Moura, Jr., M. Quintano, J. J. Antonio, M. Freindorf, and E. Kraka, Automatic generation of local vibrational mode parameters: From small to large molecules and QM/MM systems, J. Phys. Chem. A **126**, 9313 (2022).

[70] P. B. Allen, Theory of thermal expansion: Quasi-harmonic approximation and corrections from quasi-particle renormalization, Mod. Phys. Lett. B **34**, 2050025 (2020).

[71] A. Erba, On combining temperature and pressure effects on structural properties of crystals with standard *ab initio* techniques, J. Chem. Phys. **141**, 124115 (2014).

[72] A. Erba, M. Shahrokhi, R. Moradian, and R. Dovesi, On how differently the quasi-harmonic approximation works for two isostructural crystals: Thermal properties of periclase and lime, J. Chem. Phys. **142**, 044114 (2015).

[73] A. Erba, J. Maul, M. De La Pierre, and R. Dovesi, Structural and elastic anisotropy of crystals at high pressures and temperatures from quantum mechanical methods: The case of Mg_2SiO_4 forsterite, J. Chem. Phys. **142**, 204502 (2015).

[74] A. Erba, J. Maul, R. Demichelis, and R. Dovesi, Assessing thermochemical properties of materials through *ab initio* quantum-mechanical methods: The case of α-Al_2O_3, Phys. Chem. Chem. Phys. **17**, 11670 (2015).

[75] A. Erba, J. Maul, M. Itou, R. Dovesi, and Y. Sakurai, Anharmonic thermal oscillations of the electron momentum distribution in lithium fluoride, Phys. Rev. Lett. **115**, 117402 (2015).

[76] J. Maul, I. Santos, J. Sambrano, and A. Erba, Thermal properties of the orthorhombic $CaSnO_3$ perovskite under pressure from *ab initio* quasi-harmonic calculations, Theor. Chem. Acc. **135**, 36 (2016).

[77] A. Erba, J. Maul, and B. Civalleri, Thermal properties of molecular crystals through dispersion-corrected quasi-harmonic *ab initio* calculations: The case of urea, Chem. Commun. **52**, 1820 (2016).

[78] M. T. Ruggiero, J. A. Zeitler, and A. Erba, Intermolecular anharmonicity in molecular crystals: Interplay between experimental low-frequency dynamics and quantum quasi-harmonic simulations of solid purine, Chem. Commun. **53**, 3781 (2017).

[79] C. Adamo and V. Barone, Toward reliable density functional methods without adjustable parameters: The PBE0 model, J. Chem. Phys. **110**, 6158 (1999).

[80] S. Grimme, J. Antony, S. Ehrlich, and H. Krieg, A consistent and accurate *Ab-Initio* parametrization of density functional dispersion correction (DFT-D) for the 94 Elements H-Pu, J. Chem. Phys. **132**, 154104 (2010).

[81] D. Vilela Oliveira, J. Laun, M. F. Peintinger, and T. Bredow, BSSE-Correction scheme for consistent Gaussian basis sets of double- and triple-zeta valence with polarization quality for solid-state calculations, J. Comput. Chem. **40**, 2364 (2019).

[82] R. Dovesi, V. Saunders, C. Roetti, R. Orlando, C. Zicovich-Wilson, F. Pascale, B. Civalleri, K. Doll, N. Harrison, I. Bush, *et al.*, Crystal23 (unpublished).

[83] K. Doll, Analytical stress tensor and pressure calculations with the crystal code, Mol. Phys. **108**, 223 (2010).

[84] S. Casassa, A. Erba, J. Baima, and R. Orlando, Electron density analysis of large (molecular and periodic) systems: A parallel implementation, J. Comput. Chem. **36**, 1940 (2015).

[85] A. Cossard, J. K. Desmarais, S. Casassa, C. Gatti, and A. Erba, Charge density analysis of actinide compounds from the quantum theory of atoms in molecules and crystals, J. Phys. Chem. Lett. **12**, 1862 (2021).

[86] A. Cossard, S. Casassa, C. Gatti, J. K. Desmarais, and A. Erba, Topology of the electron density and of its laplacian from periodic LCAO calculations on f-electron materials: The case of Cesium uranyl chloride, Molecules **26**, 4227 (2021).

[87] See Supplemental Material at http://link.aps.org/supplemental/10.1103/f9bp-9ggw for (i) preliminary results on the effect of different exchange-correlation functionals, (ii) a graphical representation of the normal modes of selected spectral features in the IR and Raman spectra, and (iii) an analysis of the intensity of peaks in the THz region of the Raman spectrum of $Mg(IO_3)_2$.

[88] A. Liang, C. Popescu, F.-J. Manjón, R. Turnbull, E. Bandiello, P. Rodriguez-Hernandez, A. MunÃÉoz, I. Yousef, Z. Hebboul, and D. Errandonea, Pressure-Driven symmetry-preserving phase transitions in $Co(IO_3)_2$, J. Phys. Chem. C **125**, 17448 (2021).

[89] J. Maul, A. Erba, I. Santos, J. Sambrano, and R. Dovesi, In silico infrared and Raman spectroscopy under pressure: The case of $CaSnO_3$ perovskite, J. Chem. Phys. **142**, 014505 (2015).

[90] M. Veithen, X. Gonze, and P. Ghosez, Nonlinear optical susceptibilities, Raman efficiencies, and electro-optic tensors from first-principles density functional perturbation theory, Phys. Rev. B **71**, 125107 (2005).

[91] J. Maul, D. Mitoli, A. Erba, and R. P. S. Dutra, Atomistic insights on the elasticity and Raman spectra of C-S-H from quantum-mechanical simulations, J. Am. Ceram. Soc. **109**, e70399 (2026).